RSC Advances

PAPER

View Article Online
View Journal | View Issue

Cite this: *RSC Adv.*, 2023, **13**, 743

PdO@$CoSe_2$ composites: efficient electrocatalysts for water oxidation in alkaline media†

Abdul Hanan, [a] Muhammad Yameen Solangi, [b] Abdul Jaleel laghari, [b] Aqeel Ahmed Shah,[c] Umair Aftab, *[b] Zahoor Ahmed Ibupoto,[j] Muhammad Ishaque Abro,[b] Muhammad Nazim Lakhan,[a] Irfan Ali Soomro,[d] Elmuez A. Dawi,[e] Abd Al Karim Haj Ismail,[e] Elfatih Mustafa, [f] Brigitte Vigolo, [h] Aneela Tahira[i] and Zafar Hussain Ibupoto *[g]

In this study, we have prepared cobalt selenide ($CoSe_2$) due to its useful aspects from a catalysis point of view such as abundant active sites from Se edges, and significant stability in alkaline conditions. $CoSe_2$, however, has yet to prove its functionality, so we doped palladium oxide (PdO) onto $CoSe_2$ nanostructures using ultraviolet (UV) light, resulting in an efficient and stable water oxidation composite. The crystal arrays, morphology, and chemical composition of the surface were studied using a variety of characterization techniques, including X-ray diffraction (XRD), scanning electron microscopy (SEM), high resolution transmission electron microscopy (HRTEM), X-ray photoelectron spectroscopy (XPS), and Fourier transform infrared (FTIR) spectroscopy. It was also demonstrated that the composite systems were heterogeneous in their morphology, undergoing a shift in their diffraction patterns, suffering from a variety of metal oxidation states and surface defects. The water oxidation was verified by a low overpotential of 260 mV at a current density of 20 mA cm^{-2} with a Tafel Slope value of 57 mV dec^{-1}. The presence of multi metal oxidation states, rich surface edges of Se and favorable charge transport played a leading role towards water oxidation with a low energy demand. Furthermore, 48 h of durability is associated with the composite system. With the use of PdO and $CoSe_2$, new, low efficiency, simple electrocatalysts for water catalysis have been developed, enabling the development of practical energy conversion and storage systems. This is an excellent alternative approach for fostering growth in the field.

Received 18th November 2022
Accepted 16th December 2022

DOI: 10.1039/d2ra07340d

rsc.li/rsc-advances

1. Introduction

Fossil fuel use has negatively impacted the environment and led to massive environmental challenges due to greenhouse gas production.[1–3] Along with the environmental issues caused by fossil fuel combustion, their reservoirs are rapidly being depleted, posing a strong and acute threat to life on earth. It is therefore necessary to eliminate greenhouse gases by reducing or eliminating fossil fuel use, and to produce green fuels with renewable aspects for current and future uses.[4,5] Hydrogen energy has been used to build Fuel Cell technology.[6,7] In the future, hydrogen and oxygen fuels could be readily obtained for the fulfillment of energy demands through water splitting.[8,9] Water splitting can produce hydrogen and oxygen gases using either photochemical or electrochemical methods. Water splitting requires both water oxidation and hydrogen evolution reactions (HER) to be driven by efficient catalytic materials. The pre-requirement for the use of both methods for water splitting is the efficient catalytic material to drive water oxidation and HER. It is challenging from a kinetics perspective to oxidize water since four electrons are transferred, and the HER is the simplest process as only two electrons are transferred.[10,11]

[a]*Key Laboratory of Superlight Material and Surface Technology, Ministry of Education, College of Materials Science and Chemical Engineering, Harbin Engineering University, 150001, Harbin, PR China*

[b]*Department of Metallurgy and Materials Engineering, Mehran University of Engineering and Technology, 76080, Jamshoro, Pakistan. E-mail: umair.aftab@faculty.muet.edu.pk*

[c]*NED University of Engineering and Technology, 75270, Karachi, Pakistan*

[d]*Institute of Computational Chemistry, College of Chemistry, Beijing University of Chemical Technology, 100029, Beijing, PR China*

[e]*Nonlinear Dynamics Research Centre (NDRC), Ajman University, P.O. Box 346, United Arab Emirates*

[f]*Department of Science and Technology (ITN), Linköping University, Campus Norrköping, 60174 Norrköping, Sweden*

[g]*Dr M. A. Kazi Institute of Chemistry University of Sindh, Jamshoro, 76080, Pakistan. E-mail: zaffar.ibhupoto@usindh.edu.pk*

[h]*Université de Lorraine, CNRS, IJL, F-54000 Nancy, France*

[i]*Institute of Chemistry, Shah Abdul Latif University Khairpur Mirs, Sindh, Pakistan*

[j]*Faculty of Agricultural Engineering and Technology, PMAS-Arid Agriculture University, Rawalpindi, Pakistan*

† Electronic supplementary information (ESI) available. See DOI: https://doi.org/10.1039/d2ra07340d

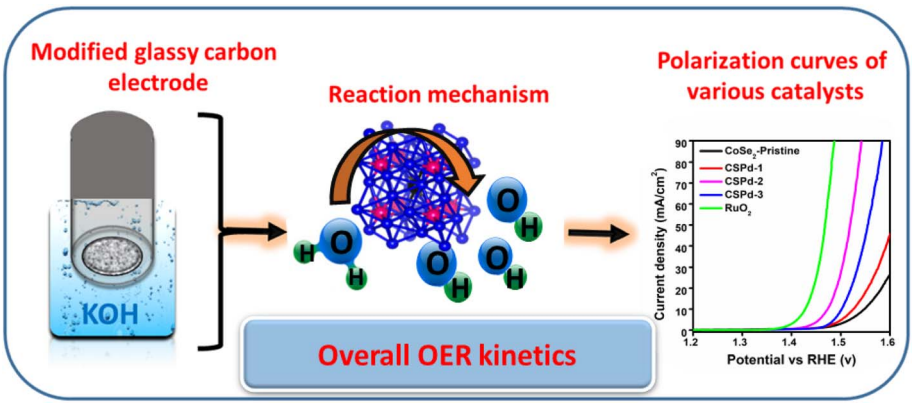

Scheme 1 Illustration of OER functional surface properties of as-prepared materials.

Nevertheless, water oxidation is only limited by the use of precious electro catalysts such as RuO_2 and IrO_2.[12–14] Rare abundance and high costs limit the use of these noble materials,[15,16] indicating that new efficient and cost effective electrocatalyst technology is in need for water oxidation. Numerous studies have been conducted to find low-cost and earth-abundant electrocatalysts that foster water oxidation.[17,18] Various transition-metal based oxides,[19,20] sulfides,[21,22] phosphides,[23,24] selenides[25] electrocatalysts for water oxidation have been reported. Extensive studies have been performed for the development of efficient, facile, stable and earth abundant electrocatalysts for the hydrogen production due the fact that the complete exploitation of hydrogen fuel from water splitting is restricted by high energy demanding half-cell water oxidation reaction. As water oxidation is followed by the four-electron transfer reaction, an effective material is needed to drive significant water oxidation with low energy requirements (Scheme 1).

As a result of the availability of multiple metal oxidation states and the unique architecture of anions as counter anions attached to these multiple metals, researchers have considered the preparation of bimetallic and polymetallic compounds for electrocatalytic applications, which have proven more effective than monometallic compounds for water oxidation.[26] In addition, recent studies indicate that metal oxides and metal selenides perform better as electrocatalysts than sulfides and phosphides of transition metals.[27–30] Selenides can serve as highly potent catalysts to overcome the above-mentioned challenges for water electrolysis. Se atoms have an electronic structure of $4s^2 4p^4$, which are easily to gain two electrons from less electronegative elements to form Se^{2-} ions, or to share electrons with more electronegative elements to form TMSes.[31] The TMSes has a high surface area due to its ultrathin layers and the surface concentration of atoms is also high, which in turn reduces the charge transfer distance thus the process of water splitting for OER gets accelerated.[32] Due to several reasons, the cobalt selenide ($CoSe_2$) based electrocatalysts are useful for water oxidation, including their low cost, simple nature, and significant electrochemical activity.[33–36]

Due to its unique synergetic properties and abundant catalytic sites, composite materials are being made in larger and larger quantities for the development of effective water oxidation electrocatalysts.[37,38] A wide range of methods have been used to synthesize cobalt-based nanostructures, including precipitation, vapor deposition, and wet chemical reactions.[39–43]

Even though the use of these methods is growing rapidly, there is still a need to adopt facile approaches for the development of new generation electrocatalysts at a large scale while incorporating the simple, scalable and tunable features of the nanostructured materials to be prepared. According to the available literature, PdO nanoparticles have not been doped into $CoSe_2$ nanostructures *via* hydrothermal methods followed by UV light reduction. The UV light offers the facile approach to synthesize highly efficient hybrid materials and it can decrease the cost of fabrication of electrocatalyst. Particularly the deposition of few amounts of precious material onto $CoSe_2$ is possible by UV light which further paved the way to the development of new generation of active electrocatalysts for OER. Because of the unique three-dimensional electronic configuration of Co and Pd, as well as the abundance of surface edge sites of Se in the composite systems, the kinetics of water oxidation are likely to be accelerated with a low energy consumption.

The present study investigated the preparation of cobalt selenide ($CoSe_2$) nanostructures by hydrothermal methods and the doping of palladium oxide (PdO) nanoparticles on them using a UV irradiation technique to synthesize a composite system represented as PdO@$CoSe_2$. Upon applying 260 mV overpotential to the PdO@$CoSe_2$ composite, a Tafel slope value of 57 mV dec^{-1} indicated that the effect had a current density of 20 mA cm^{-2}.

2. Experimental work

2.1. Chemical reagents

Cobalt chloride hexahydrate ($CoCl_2 \cdot 6H_2O$), selenium chloride ($SeCl_2$), palladium chloride ($PdCl_2$), hydrazine hydrate (N_2H_4), hydrochloric acid (HCl) and deionized water were purchased from Sigma-Aldrich. All the chemicals were of analytical category and used without any further treatments.

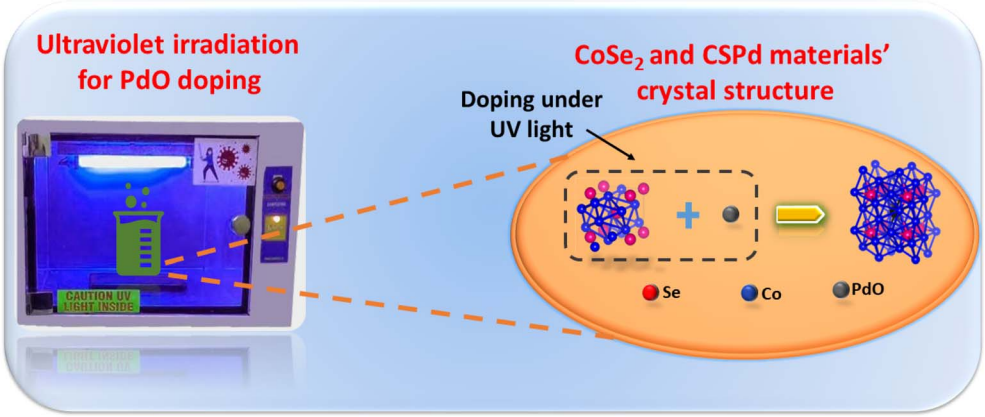

Scheme 2 Illustration of overall doping of PdO onto $CoSe_2$ nanostructures.

2.2. Synthesis of PdO@$CoSe_2$ composites

Initially, cobalt selenide ($CoSe_2$) nanostructures were synthesized using hydrothermal approach that involved dissolving 0.1 M cobalt chloride ($CoCl_2$) in deionized water (DW) and stirring for 15 minutes. Then, 0.1 M selenium chloride ($SeCl_2$) was added to above solution at room temperature under continuous stirring. Later, hydrazine (N_2H_4) aqueous was added dropwise into the solution. Then, the mixture was transferred into Teflon-lined stainless-steel autoclave and put into electric oven instrument using FOTILE 52 L at 180 °C for 15 h. The hydrothermal autoclave was cooled at room temperature and precipitates of $CoSe_2$ were collected through centrifuge instrument by 4000RPM NSL 80-1. Finally, as-obtained precipitates of $CoSe_2$ were washed by DW and dried at 50 °C for 5 h. On the other hand, palladium chloride ($PdCl_2$) solution was prepared by dissolving 30 mg into 0.02 M HCl. Three different composite samples were prepared by using 100 mg cobalt selenide ($CoSe_2$) with varying ratio of palladium (Pd) solution as 5 mL, 10 mL, and 15 mL into 100 mL of DW and marked as CSPd-1, CSPd-2, CSPd-3 respectively. Samples were placed in Ultrasonic bath for 20 min. The samples were then placed in an ultraviolet light chamber with magnetic stirring for 2 h to ensure adequate doping of PdO nanoparticles (PdNPs) on the surface of $CoSe_2$. After the completion of process, samples were taken from the UV chamber and washed several times with DW before being dried at 60 °C under vacuum conditions. Scheme 2 depicts a schematic representation of PdO nanoparticles doping onto $CoSe_2$ under UV irradiation.

2.3. Characterization

The composition and crystalline arrays of prepared nanostructures were analyzed by using X-ray diffraction (XRD) instrument by RIGAKU TTR at accelerating rate of 45 kV and current of 45 mA with intensity of Cu Kα radiation ($\lambda = 0.15406$ nm). The morphology was analyzed through scanning electron microscopy (SEM) instrument by JEOL JSM-6380LV with operating voltage of 20 kV. High resolution transmission electron microscopy (HRTEM) instrument by FEI TECHNNAI G2 (containing a Schottky emitter functioning at 200 kV) was applied for further morphological characteristics in detail. Chemical attachment of materials was analyzed by X-ray photoelectron spectroscopy (XPS) by PerkinElmer PH 5100 XPS X-ray photoelectron spectrometer system. Before deconvolution by CasaXPS, the spectra have been calibrated to C 1s at 285 eV. The background was a Shirley curve and for the XPS features, Voigt curves were used. The Fourier transform infra-red (FTIR) instrument by PerkinElmer was applied for understanding the chemical bonding features of PdO@$CoSe_2$ composites. UV aging test chamber model no NKHS-UV was used with set parameters such as irradiation intensity of 0–2.0 W m^{-2}/340 nm, UV wavelength range 290–400 nm, and lamp power of L = 1200/40 W/8 pcs during synthesis process.

2.4. Electrochemical measurements

Various electrochemical measurements were performed in 1.0 M potassium hydroxide (KOH) solution using potentiostat by VERSASTAT4-500, including linear sweep voltammetry (LSV), electrochemical impedance spectroscopy (EIS), cyclic voltammetry (CV), and chronopotentiometry. Various electrochemical tests were performed using a three-electrode cell system with a modified glassy carbon electrode (GCE) as working electrode, a silver–silver chloride (Ag/AgCl) filled with 3 M potassium chloride (KCl) solution as the reference electrode, and a platinum wire as the counter electrode. Dissolving or 5 mg of each prepared catalyst (CSPd material) in 10 mL of DW and 0.1 mL of 5% Nafion solution yielded the necessary catalytically material ink. The intended electro-catalytical slurry was based on four separate elements: pure $CoSe_2$, PdO@$CoSe_2$ composites, and ruthenium oxide (RuO_2). Before testing, a homogeneous slurry was obtained by continuously stirring in an ultrasonic bath for 20–30 minutes. Each catalyst was dropped with 5 μL onto the cleaned GCE surface (with 3 mm contact area) and dried at room temperature using an air blower. The mass of catalyst deposited onto GCE working electrode was determined to be roughly 0.2 mg. First LSV was used to examine the polarization curves for water oxidation. The EIS was used to examine the charge transfer resistance for each catalyst, with experimental conditions of sweeping frequency ranging from 100 kHz to

0.1 Hz, a sinusoidal potential of 5 mV, and 1.45 V *versus* RHE (water oxidation onset potential). The EIS raw data was simulated by Z-view software. The durability of the as-prepared catalyst was tested for 48 h at three different current densities of 20, 40, and 60 mA cm^{-2}. The electrochemical active surface area (ECSA) was estimated non-faradic zone of CV curves obtained at various scan rates. The Nernst equation was used to report Ag–AgCl reference potential into reversible hydrogen electrode (RHE) potential

$$E_{RHE} = E_{Ag/AgCl} + 0.059\ pH + E^{\circ}_{Ag/AgCl}$$

where $E^{\circ}_{Ag/AgCl}$ is 0.2412 and overpotential (η) is received by subtracting onset thermodynamic potential of 1.23 V for water splitting system.

$$\text{Overpotential } (\eta) = \text{onset potential } (E_{RHE})\ V - 1.23\ V$$

However, the Tafel slope was calculated by using Tafel equation.

$$\eta = b \log j + a$$

where η is overpotential, b is Tafel slope and j is current density.

3. Results and discussion

3.1. Crystal arrays, morphology, chemical composition and surface analysis of as prepared PdO@$CoSe_2$ composites

The powder X-ray diffraction (XRD) patterns were collected to investigate the crystallographic perspectives of several electrocatalytical materials, including pure cobalt selenide ($CoSe_2$) and their composites with palladium oxide (PdO) labeled as CSPd-1, CSPd-2, and CCSPd-3. Based on the JCPDS 00-010-0409 reference card number, pure $CoSe_2$ demonstrated a cubic crystal structure, confirming successful synthesis (Fig. 1(a)). Furthermore, several composites of $CoSe_2$ with PdO exhibited similar cubic diffraction patterns based on the reference card number (JCPDS: 0303-065-5065). As shown by the card number (JCPDS: 03-065-5065), PdO is successfully doped in a cubic

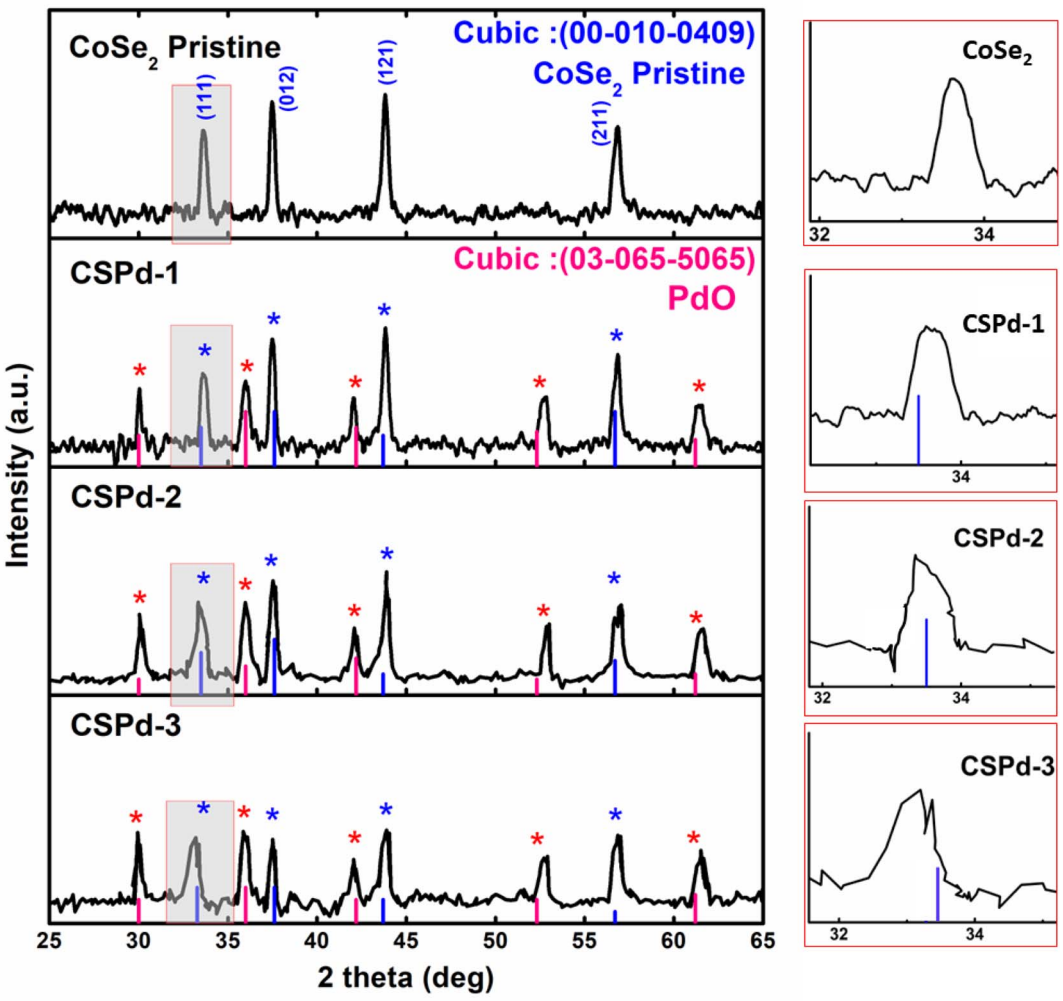

Fig. 1 X-ray diffraction patterns of various samples such as pure and $CoSe_2$, CSPd-1, CSPd-2 and CSPd-3 composites.

phase as evidenced by the reflections of PdO. In Fig. 1, a magnified view shows peak shifting that can be seen clearly on the right side. $CoSe_2$ nanostructures were also amended with PdO nanoparticles, which changed lattice positions and introduced additional stresses (compressive) as previously shown.[44,45] As a result of stress, the position of the lattice (111)

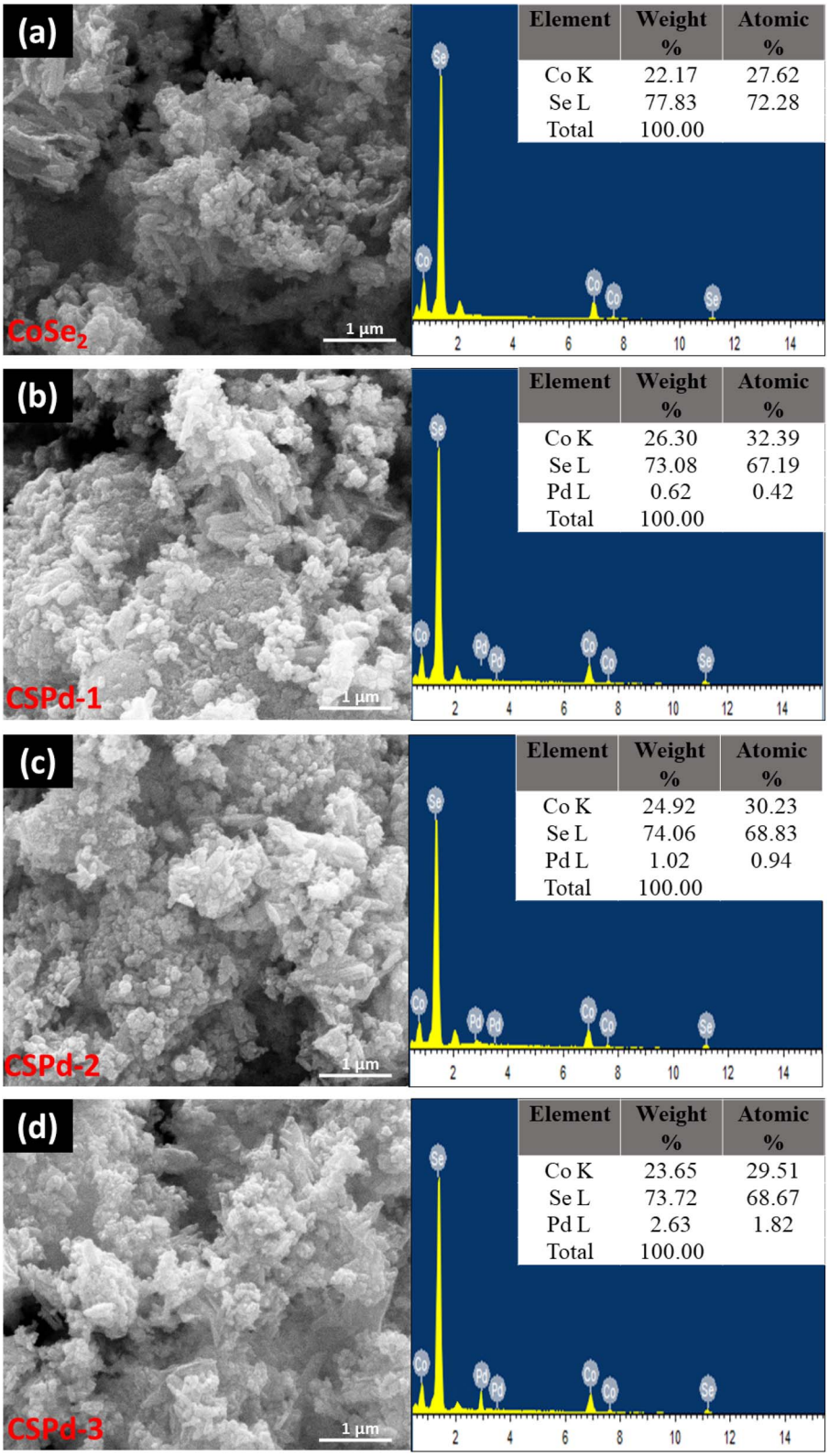

Fig. 2 SEM and EDS spectra of different nanostructures (a) $CoSe_2$ (b) CSPd-1 (c) CSPd-2 and (d) CSPd-3.

has changed kinetically which is red highlighted and clearly shown with magnification on the right side of Fig. 1. Moreover, HRTEM calculations of lattice fringes were used to validate diffraction patterns. It was not found that the composite systems contained any further peaks or other impurities based on the results of XRD analysis.

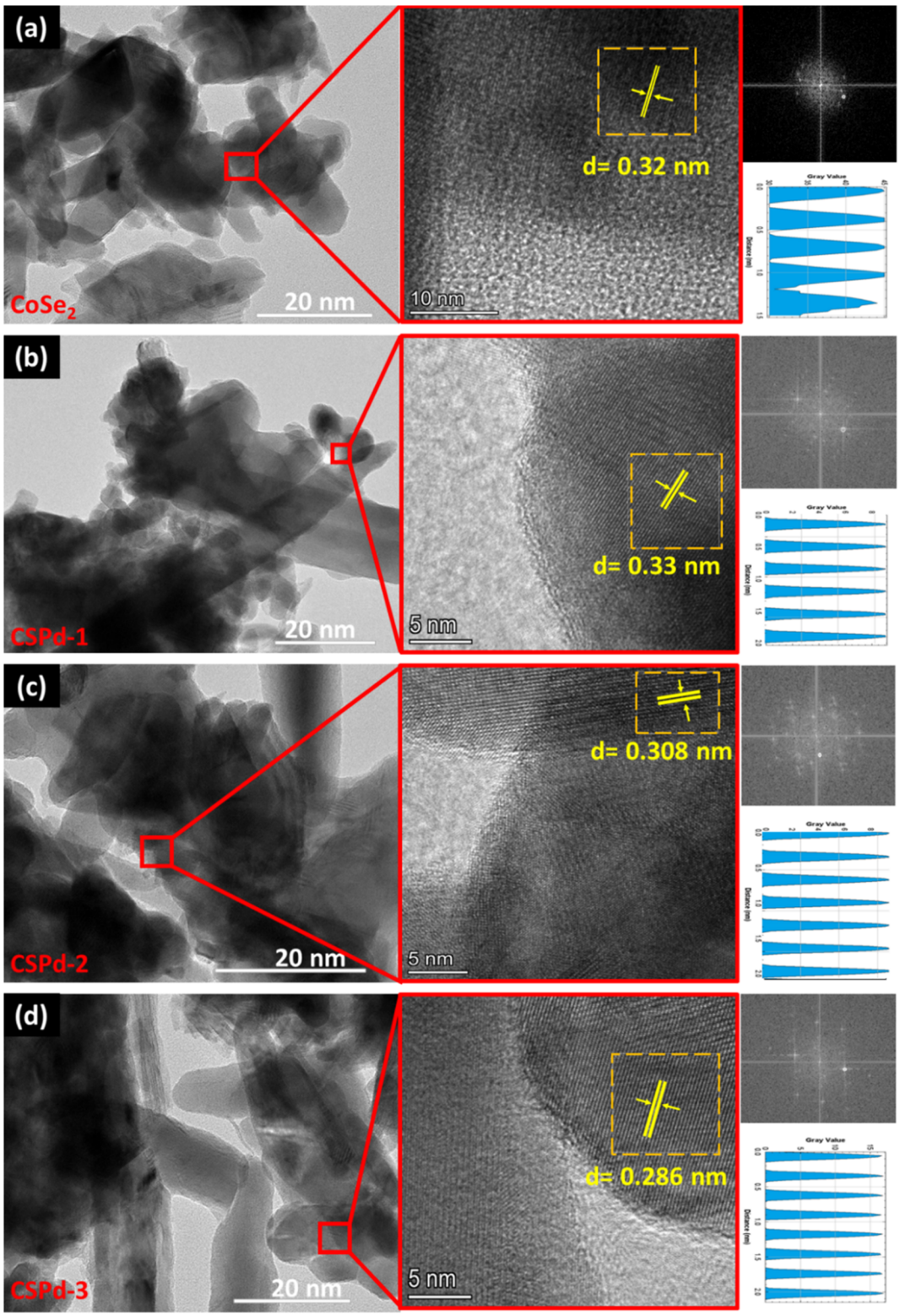

Fig. 3 HRTEM images of various nanostructures along with their FFT and lattice fringes calculation (a) $CoSe_2$ (b) CSPd-1 (c) CSPd-2 and (d) CSPd-3.

We examined the morphologies of pristine $CoSe_2$ and its composites with PdO nanoparticles by SEM imaging and elucidated their elemental compositions by EDS spectra, Fig. 2.

The $CoSe_2$ nanostructures were characterized with sharp edges topical surface shapes and a lumpy morphology.[46,47] Aside from the physical morphology of $CoSe_2$, its chemical composition has been confirmed by EDS spectrum as shown from right side of Fig. 2(a) and only Co and Se elements were identified. Additionally, the as-prepared composite nanostructures had slightly heterogeneous morphologies characterized by sharp edges aggregating with PdO nanoparticles Fig. 2(b)–(d), respectively.[48,49] An EDS analysis of composite systems revealed that Pd was present along with Co and Se elements in very small quantities. We have performed an elemental mapping to describe the distribution of various elements in pure $CoSe_2$ and composite systems as shown in ESI Fig. S1 and S2.† According to both SEM and EDS analysis, PdO has successfully been doped on $CoSe_2$ and the morphology has been slightly changed as evidenced by the presence of Co, Se, and Pd elements. TEM analysis was also performed to obtain localized information at the atomic level for pure $CoSe_2$ and its composite samples like CSPd-1, CSPd-2, and CSPd-3 for viewing and understanding the lattice fringes within the samples. On the right side of Fig. 3, Fast Fourier Transform (FFT) images are shown for each sample. As shown in Fig. 3(a), pure $CoSe_2$ nanostructures have lumpy shapes and are highly consistent with SEM results. $CoSe_2$ was found to have a *d*-spacing of 0.32 nm in the pure sample, as previously demonstrated.[50,51]

The morphologies of as-prepared composite materials such as CSPd-1, CSPd-2 and CSPd-3 are depicted in Fig. 3(b)–(d) along with *d*-spacing values respectively. The FFT analysis has shown the *d*-spacing values as 0.33, 0.308, and 0.208 nm for SPd-1, CSPd-2 and CSPd-3.[52] The *d*-spacing values suggest that the materials are well defined by the nanostructured phase and with excellent crystalline qualities.[53,54]

The chemical state and surface composition of various materials have been examined using X-ray photoelectron spectroscopy (XPS) as shown in Fig. 4. The Co 2p photoelectron signals of pure $CoSe_2$ can be seen in Fig. 4(a). It shows four doublets corresponding to Co $2p_{3/2}$ and Co $2p_{1/2}$ contributions and the relevant spectra matched with the previously reported cobalt spinel phase.[47,55] However, the peak at 779.46 eV corresponds to Co^{3+}, peak at 780.87 eV is in-tune-with Co^{2+} and the signal at 785.51 eV represents Co^{2+} in $Co(OH)_2$.[35] As shown in Fig. 4(c), the binding energy between the two materials has somewhat altered. As with Fig. 4(b) and (d), the Se 3d has two high binding energy contributions at 60.11 eV and 62.00 eV coming from selenium–oxygen bonds probably located at the

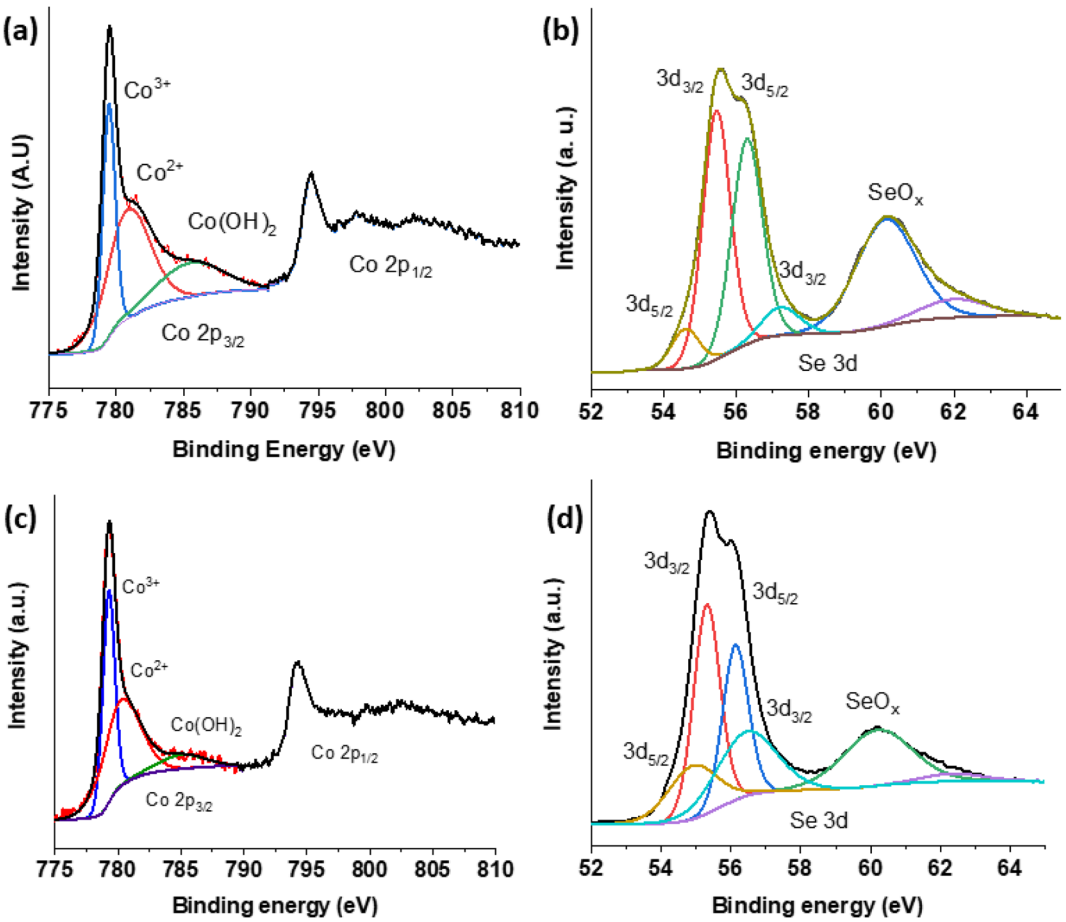

Fig. 4 XPS spectra of various nanostructures $CoSe_2$; (a) Co 2p (b) Se 3d and CSPd-2; (c) Co_2 (d) Se 3d.

catalyst surface.[56] Additionally, two peaks at 54.60 eV and 56.29 eV correspond to Se $3d_{3/2}$ and 55.45 eV and 57.22 eV correspond to Se $3d_{5/2}$ feature. These latter are due to selenium–metal bonding structure as well.[56] For CSPd-2, Co 2p, Se 3d and Pd 3d are shown in Fig. 4(c)–(e). Similarly, to $CoSe_2$ (Fig. 4(a)), Co 2p of CSPd-2 shows Co^{3+}, Co^{2+} and hydroxylated cobalt contributions at around 779.28 eV, 780.27 eV and 785.04 eV (Fig. 4(c)). Regarding Se 3d feature of CSPd-2 (Fig. 4(d)), the binding energy of Se–metal contributions are located at 54.88 eV and 56.13 eV for Se $3d_{3/2}$ and 55.33 eV and 56.44 eV for Se $3d_{5/2}$ feature. The higher binding energy contributions at 60.20 eV and 62.34 eV are assigned to selenium–oxygen bonds. Pd 3d peaks have been observed from sample CSPd-2 which revealed the two main peaks at 337.24 eV and 342.53 eV, can be assigned to Pd $3d_{5/2}$ and Pd $3d_{3/2}$ respectively,[57] as shown Fig. S3(a).† Furthermore, ESI Fig. S3(b)† illustrates the XPS survey spectrum of CSPd-2.

The Fourier transform infrared (FTIR) of several samples can be seen in ESI Fig. S4.† Using this technique, it is possible to confirm the presence of characteristic vibrations and functional groups in the samples. In line with related research, the broader bands observed at 3300–3400 cm^{-1} and 1400 to 1500 cm^{-1} are likely caused by OH^- stretching and adsorbed water molecules at the surface of samples due to moisture absorption.[58] The fundamental characteristic vibrational modes of Co–Se bonding could be assigned to bands ranging from 500 to 900 cm^{-1}.[59] The parallel $cCoSe_2$ nanostructures show decreased band structure due to cobalt and selenium vibrating at different frequencies.[60] As a result of the presence of PdO into $CoSe_2$, the broader peak at 875 cm^{-1} has been lowered, and a little hump can be seen in CSPd-3 as a result of Pd.[61] An analysis of the FTIR spectrum confirmed the development of pure $CoSe_2$ and composite nanostructures.

3.2. Electrochemical performance of PdO@$CoSe_2$ for water oxidation

The electrochemical half-cell characterization for water oxidation was carried with LSV at 2 mV s^{-1} polarization curves for pristine $CoSe_2$, CSPd-1, CSPd-2, and CSPd-3 composites, and Ruthenium Oxide (RuO_2) in 1 M KOH as shown in Fig. 5(a). The measured overpotentials for pure $CoSe_2$, CSPd-1, CSPd-2, and CSPd-3, are 350, 320, 260, and 290 mV at 20 mA cm^{-2} respectively. The pure $CoSe_2$ sample has exhibited large overpotential, indicating that the material has capability to show activity for OER reaction, however its high energy barrier is the main challenge due to its few active sites, and poorly organized surface properties. Whereas the composite CSPd-1 has described relatively lower energy barrier for OER and the composite CSPd-2 has the lowest overpotential of 260 mV at 20 mA cm^{-2}, confirming that doping of few amounts of PdO onto $CoSe_2$ can significantly reduce the energy barrier during water oxidation. First, the presented composite was identified with an optimum dose of doped PdO (CSPd-2), afterwards the decrease in activity of CSPd-3 could be connected to the agglomeration that we observed physically during the measurement on the surface of electrode. As higher doped level of PdO, there might be detachment of PdO from the surface of $CoSe_2$ during the measurement and consequently, we have observed poor performance from CSPd-3 sample. It is because the large amount of PdO that could not properly settled onto the surface of $CoSe_2$ due to high probability of incompatible factor at higher level of PdO dopant, therefore we observed the agglomeration on the surface of electrode. Hence, decrease in catalytic activity of CSPd-3 sample was noticed as shown in Fig. 5(a). For better visualization bar graph of overpotential for various materials is enclosed in Fig. 5(b). The ruthenium oxide (RuO_2) has been investigated with lower overpotential and it is being a state of art catalyst has the limitation of high cost and rare abundance, however heterostructure CSPd-2 has closely assigned overpotential and it could be used as an alternative material for large scale production of oxygen gas as a green fuel and for full exploitation of hydrogen form water splitting. The lower energy demand based on the CSPd-2 is attributed to high density of active sites, fast charge transport, defects in the crystal structure, large surface area due to nanoscale dimension, and favorable surface science owing to multi d orbital configuration.

By using the Tafel slope equation as the rate-determining step for the OER mechanism was evaluated from the linear region of LSV and the calculation was made as previous reported work,[62] as shown in the Fig. 5(c). Particularly compared to pristine $CoSe_2$ and other composite materials like CSPd-2 has low Tafel slope value of 57 mV dec^{-1} and its close to noble metal RuO_2 with a Tafel slope value of 52 mV dec^{-1}, suggesting that the proposed materials have almost swift reaction kinetics as exhibited by noble metal material. The relative lowering of Tafel slope values of tested materials were found the in the order RuO_2 < CSPd-2 < CSPd-3 < CSPd-1 < $CoSe_2$ as enclosed in Fig. 5(c).

The water oxidation is accompanied by the involvement of four electron transfer process and general steps involved in the alkaline reaction are described by the following main steps:

$$M + OH^- \rightarrow MOH + e^- \quad (1)$$

$$MOH + OH^- \rightarrow MO^-H_2O \quad (2)$$

$$MO^- \rightarrow MO + e^- \quad (3)$$

$$2MO \rightarrow 2M + O_2 + 2e^- \quad (4)$$

Theoretical Tafel analysis for the estimation of water oxidation reaction mechanism is associated with the Tafel values of 120, 60, 40, and 15 mV dec^{-1}. The proposed study is favored by the step 2 and it could, be considered as rate limiting step for water oxidation under alkaline conditions.[63–66]

It is interesting to note that electrochemical performance for as-prepared material is strongly connected to the durability of material for long term reaction. Hence, the chronopotentiometry experiment was performed to evaluate stability of as prepared CDPd-2 composite material for 48 h at various current densities such as 20, 40, and 60 mA cm^{-2}, as shown in Fig. 5(d). It is obvious that the potential drop for the set period of durability was negligible and the CSPd-2 material

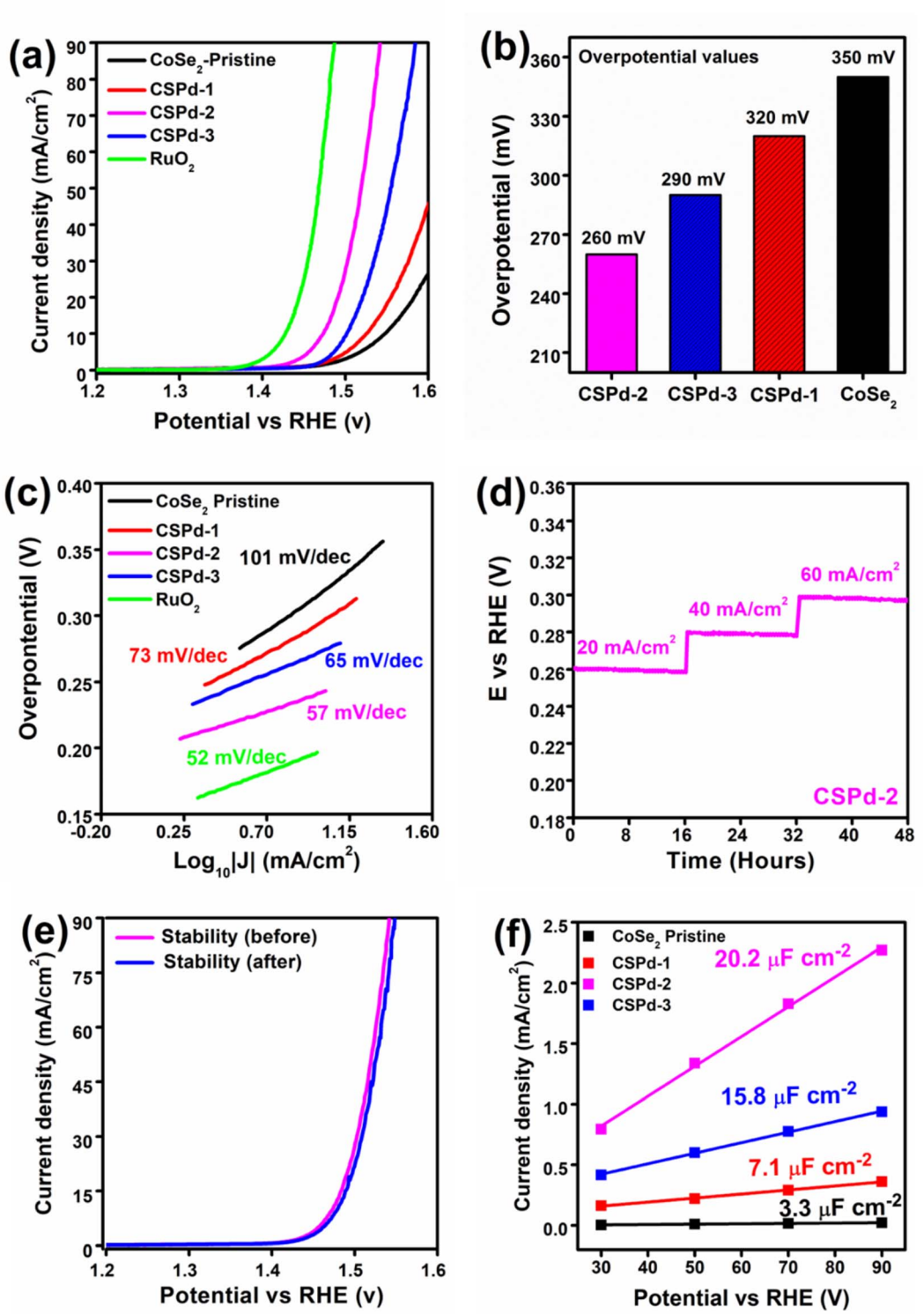

Fig. 5 (a) LSV curves of various nanostructures including $CoSe_2$, CSPd-1, CSPd-2 and CSPd-3 with reference of RuO_2 at 20 mA cm^{-2} (b) histogram of overpotential values for different catalysts (c) Tafel slope values of various materials (d) chronopotentiometry of as-prepared catalyst at different current densities such as 20, 40 and 60 mA cm^{-2} (e) durability test of CSPd-2 before and after chronopotentiometry test (f) double layer capacitance (C_{dl}) values of various catalysts, calculated at various scan rates from CV curves.

has an excellent durability as shown in Fig. 5(d) and the performance is close to the recently reported nonprecious materials.[67,68] Additionally, the stability of CSPd-2 was investigated after the durability test using LSV polarization curves before and after the stability test as shown in Fig. 5(e). The observations of stability by LSV, are highly encouraging that the material transformation and the change in the surface properties remained inactive, with outstanding stability. The

confirmation of material chemical transformation, the post SEM and EDS analysis were performed and they have shown negligible chemical change in the composition and morphological aspects, after chronopotentiometry as depicted in ESI Fig. S5.†

To examine superior OER performance, we used electrochemical active surface area (ECSA) for comparing active sites by employing non-faradaic area of CV curves at different scan rat, as shown in supplement Fig. S6† by using the following equation.

$$\mathrm{ECSA} = C_{\mathrm{dl}}/C_{\mathrm{s}}$$

where C_{s} is 0.04 mF cm^{-2} for KOH electrolyte.[69,70] The C_{dl} (double layer capacitance) is plotted as capability of sweep scan rate and linear fitting was used to determine the slope value,[71,72] as given in Fig. 5(f). The calculated value of ECSA for CSPd-2 is 310 cm^2 which is higher value than the other materials, thus it is one of the factors for the improvement of the performance of towards water oxidation.

The EIS is a necessary step in analyzing the charge transfer mechanism between electrolyte and working electrode. The Z-view software was used to simulate the raw data of EIS using an equivalent circuit as inset shown in Fig. 6 Nyquist plots were used to estimate the charge transfer resistance (R_{ct}) values of each material,[73] as enclosed in Fig. 6(a). The Bode plots have given phase features at different frequencies, shown in Fig. 6(b). Additionally, Fig. 6(c) shows the phase angle within Bode plots 65°, 42°, 24° and 19° for $CoSe_2$, CSPd-1, CSPd-3 and CSP-2 accordingly.

The R_{ct} (charge transfer resistance) values for pristine $CoSe_2$, CSPd-1, CSPd-2 and CSPd-3 were calculated as 395, 115, 47 and 87 Ω respectively which are well supported by the recently reported EIS results.[74–76] The lower charge transfer value of CSPd-2 favored quick charge transfer at the interface of electrolyte and the electrode for favorable water oxidation.

The summary of obtained electrochemical results from LSV, ECSA, and EIS analysis is given in Table 1. It is obvious that the electrochemical performance of CSPd-2 composite is superior to many the tested materials in the proposed study, hence it can be used an effective material energy conversion and energy storage systems. Furthermore, the comparative analysis in terms Tafel slope and lower overpotential of CSPd-2 was

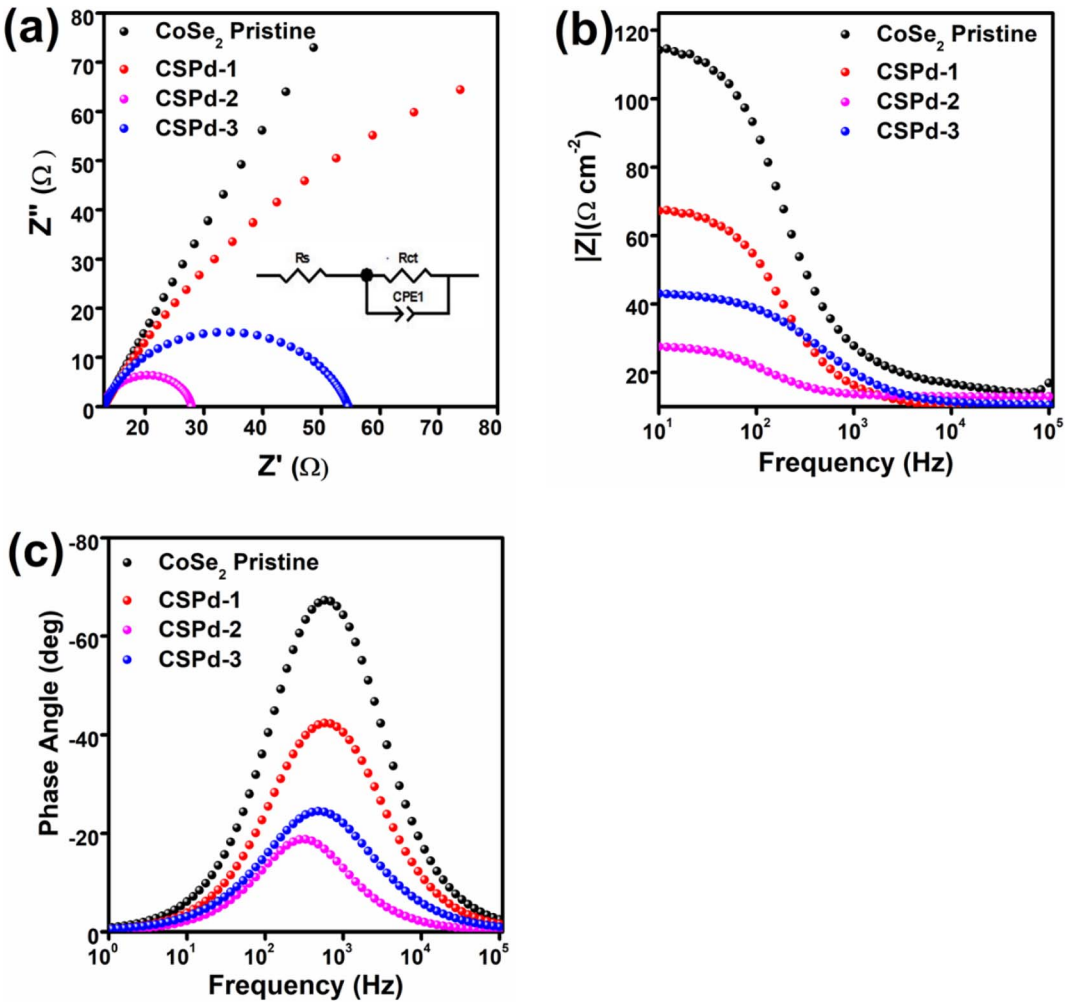

Fig. 6 (a) Corresponding Nyquist plots of dissimilar materials (b) and (c) Bode plots.

Table 1 Electrochemical Features of various electrocatalysts

	Calculation by LSV	Calculation by EIS		Calculation by CV	
	Tafel slope	Charge transfer resistance	Double layer capacitance	Double layer capacitance	Electrochemical active surface area
	B	R_{ct}	CPE_{dl}	C_{dl}	ECSA
Catalyst	mV dec^{-1}	Ω	mF	(μF cm^{-2})	cm^2
Pristine $CoSe_2$	101	395	0.04	3.8	95
CSPd-1	73	115	0.095	6.9	172
CSPd-2	57	47	0.37	12.8	320
CSPd-3	65	87	0.21	9.2	230

compared with previously reported electrocatalysts, as shown in the ESI (Table S1†). The CSPd-2 composite system has either superior or equal performance to the recently reported works in terms of low overpotential and Tafel slope. After adding the desired few amounts of PdO as contributing factor for the enhancement of water oxidation performance onto $CoSe_2$ is significantly proven as a promoter.

4. Conclusions

In summary, we attempted to doping the PdO onto $CoSe_2$ nanostructures prepared *via* wet chemical reduction using UV light. As demonstrated by SEM and HRTEM analysis, the morphology is heterogeneous, while the crystalline properties are excellent. $CoSe_2$ nanostructures were found to have PdO on their surfaces based on XRD and XPS results. The electrochemical properties of the as-prepared material towards water oxidation with low overpotential of 260 mV at a current density of 20 mA cm^{-2} and a low Tafel slope value of 57 mV dec^{-1} was observed for the CSPd-2 composite system. In addition, CSPd-2 demonstrated low charge transfer resistance R_{ct} of 47 Ω. A 48 hours durability period further validated the electrocatalytic properties of CSPd-2. The enhanced performance of CSPd-2 is attributed from the high value of ECSA, low charge transfer resistance, and synergetic effect built between the PdO, and $CoSe_2$. The evaluated performance of CSPd-2 composite sample using a small quantity of PdO played a dynamic role in the development efficient electrocatalyst and it has high window to apply for wide range of electrochemical applications such as batteries, water electrolysis, and supercapacitors.

Data availability statement

Data available in article ESI Material.†

Author contributions

Abdul Hanan, has prepared the materials, did electrocatalysis and wrote part of manuscript. Muhammad Yameen Solangi, did partial physical characterization testing. Abdul Jaleel Laghari, did Tafel analysis. Aqeel Ahmed Shah, electrochemical active surface analysis and involved in the discussion. Umair Aftab, did impedance experiment and wrote the discussion. Muhammad Ishaque Abro, partially supervised the manuscript and supported the electrochemical testing. Muhammad Nazim Lakhan, analyzed the XPS results. Irfan Ali, did all graphic materials including graphical abstract and schemes. Elmuez A. Dawi, theoretical interpretation, preparation of the manuscript. Abd Al Karim Haj Ismail, theoretical interpretation, preparation of the manuscript. Elfatih Mustafa, preparation of the manuscript. Brigitte Vigolo analyzed XPS results and edited the draft of manuscript. Aneela Tahira, analyzed the SEM and TEM results. Zafar Hussain Ibupoto, provided the hypothesis and overall supervise the work and involved manuscript.

Conflicts of interest

All authors declare no conflict of interest in this research work.

Acknowledgements

B. V. thank the platform "Microscopies, Microprobes and Metallography (3 M)" (Institut Jean Lamour, IJL, Nancy, France) for access to SEM facilities and F. Alnjiman for his valuable help. We also acknowledge partial funding of the Ajman University, Grant ID: DGSR ref. 2022-IRG-HBS-5, and we would like to thank the platform of National Natural Science Foundation of China (NSFC 51402065 and 51603053).

References

1 C. Hu, Y. Xiao, Y. Zou and L. Dai, *Electrochem. Energy Rev.*, 2018, **1**, 84–112.
2 *Nat. Rev. Chem.*, 2018, **2**, 0125.
3 S. Ghosh and R. N. Basu, *Nanoscale*, 2018, **10**, 11241–11280.
4 D. Guo, H. Kang, P. Wei, Y. Yang, Z. Hao, Q. Zhang and L. Liu, *CrystEngComm*, 2020, **22**, 4317–4323.
5 S. Ponnada, M. S. Kiai, D. B. Gorle, R. S. C. Bose, V. Rajagopal, B. Saini, M. Kathiresan, A. Nowduri, R. Singhal, F. Marken, M. A. Kulandainathan, K. K. Nanda and R. K. Sharma, *Catal. Sci. Technol.*, 2022, **12**, 4413–4441.

6 S. L. Pasarakonda, S. Ponnada, D. B. Gorle, R. S. Chandra Bose, A. Palariya, M. S. Kiai, H. B. Gandham, M. Kathiresan, R. K. Sharma and A. Nowduri, *New J. Chem.*, 2023, DOI: 10.1039/D2NJ04648B.
7 A. Shankar, R. Elakkiya and G. Maduraiveeran, *New J. Chem.*, 2020, **44**, 5071–5078.
8 H. Eidsvåg, S. Bentouba, P. Vajeeston, S. Yohi and D. Velauthapillai, *Molecules*, 2021, **26**, 1687.
9 M. Ahmed, M. N. Lakhan, A. Hanan, R. Ahmed, A. H. Shar, I. Ali, S. Mahesar, M. A. Latif, A. Muhammad and M. A. Usto, *North Am. Acad. Res. J.*, 2021, **4**(9), 19–32.
10 S. Mishra, P. Yogi, P. R. Sagdeo and R. Kumar, *ACS Appl. Energy Mater.*, 2018, **1**, 790–798.
11 A. QayoomMugheri, A. Tahira, U. Aftab, M. IshaqAbro, S. R. Chaudhry, L. Amaral and Z. H. Ibupoto, *Electrochim. Acta*, 2019, **306**, 9–17.
12 A. Sajeev, V. K. Mariappan, D. Kesavan, K. Krishnamoorthy and S.-J. Kim, *Mater. Adv.*, 2021, **2**, 455–463.
13 M. Łuba, T. Mikołajczyk, M. Kuczyński, B. Pierożyński and I. M. Kowalski, *Catalysts*, 2021, **11**, 468.
14 S. M. Galani, A. Mondal, D. N. Srivastava and A. B. Panda, *Int. J. Hydrogen Energy*, 2020, **45**, 18635–18644.
15 W. Luo, J. Gan, Z. Huang, W. Chen, G. Qian, X. Zhou and X. Duan, *Front. Mater.*, 2019, **6**, 251.
16 C. Li and J.-B. Baek, *ACS Omega*, 2020, **5**, 31–40.
17 X. Ren, Q. Lv, L. Liu, B. Liu, Y. Wang, A. Liu and G. Wu, *Sustainable Energy Fuels*, 2020, **4**, 15–30.
18 J. Peng, Y. Chen, K. Wang, Z. Tang and S. Chen, *Int. J. Hydrogen Energy*, 2020, **45**, 18840–18849.
19 R. K. Hona, S. B. Karki and F. Ramezanipour, *ACS Sustainable Chem. Eng.*, 2020, **8**, 11549–11557.
20 M. Y. Solangi, A. H. Samo, A. J. Laghari, U. Aftab, M. I. Abro and M. I. Irfan, *Int. J. Hydrogen Energy*, 2022, **5**, 32–40.
21 Y. Xue, S. Sun, Q. Wang, Z. Dong and Z. Liu, *J. Mater. Chem. A*, 2018, **6**, 10595–10626.
22 Y. Zhu, Q. Lin, Y. Zhong, H. A. Tahini, Z. Shao and H. Wang, *Energy Environ. Sci.*, 2020, **13**, 3361–3392.
23 M. Wang, L. Zhang, Y. He and H. Zhu, *J. Mater. Chem. A*, 2021, **9**, 5320–5363.
24 Y.-N. Zhou, Y.-R. Zhu, X.-Y. Chen, B. Dong, Q.-Z. Li and Y.-M. Chai, *J. Alloys Compd.*, 2021, **852**, 156810.
25 H. Du, R.-M. Kong, X. Guo, F. Qu and J. Li, *Nanoscale*, 2018, **10**, 21617–21624.
26 P. Li and H. C. Zeng, *ACS Appl. Mater. Interfaces*, 2019, **11**, 46825–46838.
27 X. Xia, L. Wang, N. Sui, V. L. Colvin and W. W. Yu, *Nanoscale*, 2020, **12**, 12249–12262.
28 Y. Xue, G. Ma, X. Wang, M. Jin, E. M. Akinoglu, D. Luo and L. Shui, *ACS Appl. Mater. Interfaces*, 2021, **13**, 7334–7342.
29 M. Jahan, Z. L. Liu and K. P. Loh, *Adv. Funct. Mater.*, 2013, **23**, 5363–5372.
30 G. Mei, H. F. Liang, B. B. Wei, H. H. Shi, F. W. Ming, X. Xu and Z. C. Wang, *Electrochim. Acta*, 2018, **290**, 82–89.
31 Z. W. Fang, L. L. Peng, H. F. Lv, Y. Zhu, C. S. Yan, S. Q. Wang, P. Kalyani, X. J. Wu and G. H. Yu, *ACS Nano*, 2017, **11**, 9550–9557.
32 F. O. Boakye, Y. Li, K. A. Owusu, I. S. Amiinu, Y. P. Cheng and H. N. Zhang, *Mater. Chem. Phys.*, 2022, **275**, 125201.
33 I. M. Abdullahi, J. Masud, P.-C. Ioannou, E. Ferentinos, P. Kyritsis and M. Nath, *Molecules*, 2021, **26**, 945.
34 J. Masud, A. T. Swesi, W. P. Liyanage and M. Nath, *ACS Appl. Mater. Interfaces*, 2016, **8**, 17292–17302.
35 L. Xia, H. Song, X. Li, X. Zhang, B. Gao, Y. Zheng, K. Huo and P. K. Chu, *Front. Chem.*, 2020, **8**, 382.
36 J. Sun, J. Li, Z. Li, X. Hu, H. Bai and X. Meng, *ACS Sustainable Chem. Eng.*, 2022, **10**, 4022–4030.
37 X. Zheng, J. Zhang, J. Wang, Z. Zhang, W. Hu and Y. Han, *Sci. China Mater.*, 2020, **63**, 347–355.
38 X. Cao, J. E. Medvedeva and M. Nath, *ACS Appl. Energy Mater.*, 2020, **3**, 3092–3103.
39 Z. Feng, B. Gao, L. Wang, H. Zhang, P. Lu and P. Xing, *J. Electrochem. Soc.*, 2020, **167**, 134501.
40 L. Shreenivasa, S. Ashoka, K. Yogesh, A. Syed, N. Marraiki and P. S. Adarakatti, *Solid State Sci.*, 2022, **124**, 106803.
41 J. Saha, S. Verma, R. Ball, C. Subramaniam and R. Murugavel, *Small*, 2020, **16**, 1903334.
42 S. Saddeler, G. Bendt, S. Salamon, F. T. Haase, J. Landers, J. Timoshenko, C. Rettenmaier, H. S. Jeon, A. Bergmann, H. Wende, B. R. Cuenya and S. Schulz, *J. Mater. Chem. A*, 2021, **9**, 25381–25390.
43 J. X. Flores-Lasluisa, F. Huerta, D. Cazorla-Amoros and E. Morallon, *Nanomaterials*, 2020, **10**(12), 2394.
44 M. Y. Solangi, U. Aftab, A. Tahira, M. I. Abro, R. Mazarro, V. Morandi, A. Nafady, S. S. Medany, A. Infantes-Molina and Z. H. Ibupoto, *Int. J. Hydrogen Energy*, 2022, **47**, 3834–3845.
45 A. Nakrela, N. Benramdane, A. Bouzidi, Z. Kebbab, M. Medles and C. Mathieu, *Results Phys.*, 2016, **6**, 133–138.
46 H. Liu, K. Xiang, B. Yang, X. Xie, D. Wang, C. Zhang, Z. Liu, S. Yang, C. Liu, J. Zou and L. Chai, *Environ. Sci. Pollut. Res.*, 2017, **24**, 14249–14258.
47 L. Zhao, J. Jia, Y. Chang, M. Jia and Z. Wen, *Int. J. Hydrogen Energy*, 2019, **44**, 22787–22795.
48 H. Wang, S. Zhang, S. Li and J. Qu, *Anal. Methods*, 2018, **10**, 1331–1338.
49 A. Zhou, R.-M. Guo, J. Zhou, Y. Dou, Y. Chen and J.-R. Li, *ACS Sustainable Chem. Eng.*, 2018, **6**, 2103–2111.
50 D. S. Gavhane, H. van Gog, B. Thombare, G. Lole, L. Christiaan Post, M. A. More and M. A. van Huis, *npj 2D Mater. Appl.*, 2021, **5**, 24.
51 G. Zhao, P. Li, K. Rui, Y. Chen, S. X. Dou and W. Sun, *Chemistry*, 2018, **24**, 11158–11165.
52 V.-D. Le, T. C.-H. Le, V.-T. Chau, T. N.-D. Le, C.-H. Dang, T. T.-N. Vo, T. D. Nguyen and T.-D. Nguyen, *New J. Chem.*, 2021, **45**, 4746–4755.
53 S. Sarkar and S. C. Peter, *Inorg. Chem. Front.*, 2018, **5**, 2060–2080.
54 T. Shen, J. Zhang, K. Chen, S. Deng and D. Wang, *Energy Fuels*, 2020, **34**, 9137–9153.
55 M. C. Biesinger, B. P. Payne, A. P. Grosvenor, L. W. M. Lau, A. R. Gerson and R. S. C. Smart, *Appl. Surf. Sci.*, 2011, **257**, 2717–2730.

56 X. Wang, Y. Xie, B. Bateer, K. Pan, X. Zhang, J. Wu and H. Fu, *ACS Sustainable Chem. Eng.*, 2019, **7**, 2784–2791.
57 Q.-S. Jiang, W. Li, J. Wu, W. Cheng, J. Zhu, Z. Yan, X. Wang and Y. Ju, *J. Mater. Sci.: Mater. Electron.*, 2019, **30**, 9429–9437.
58 B. Jansi Rani, G. Ravi, R. Yuvakkumar, B. Saravanakumar, M. Thambidurai, C. Dang and D. Velauthapillai, *ACS Omega*, 2020, **5**, 14702–14710.
59 Y. R. Zheng, M. R. Gao, Q. Gao, H. H. Li, J. Xu, Z. Y. Wu and S. H. Yu, *Small*, 2015, **11**, 182–188.
60 S. Swathi, B. J. Rani, R. Yuvakkumar, G. Ravi, E. S. Babu, M. Pannipara, A. G. Al-Sehemi and D. Velauthapillai, *Appl. Nanosci.*, 2021, **11**, 1367–1378.
61 H. Mansouri-Torshizi, E. Rezaei, F. Kamranfar and M. Heidari Majd, *Adv. Pharm. Bull.*, 2016, **6**, 449–453.
62 T. Shinagawa, A. T. Garcia-Esparza and K. Takanabe, *Sci. Rep.*, 2015, **5**, 13801.
63 Z. H. Ibupoto, A. Tahira, A. A. Shah, U. Aftab, M. Y. Solangi, J. A. Leghari, A. H. Samoon, A. L. Bhatti, M. A. Bhatti, R. Mazzaro, V. Morandi, M. I. Abro, A. Nafady, A. M. Al-Enizi, M. Emo and B. Vigolo, *Int. J. Hydrogen Energy*, 2022, **47**, 6650–6665.
64 S.-J. Huang, S. Balu, N. R. Barveen and R. Sankar, *Colloids Surf., A*, 2022, 130024.
65 C. Zhou, X. Han, F. Zhu, X. Zhang, Y. Lu, J. Lang, X. Cao and H. Gu, *Int. J. Hydrogen Energy*, 2022, **47**, 27775–27786.
66 A. Samo, U. Aftab, D. Cao, M. Ahmed, M. Lakhan, V. Kumar, A. Asif and A. J. D. J. o. N. Ali, *Dig. J. Nanomater. Biostructures*, 2022, **17**(1), 109–120.
67 T. Reier, M. Oezaslan and P. Strasser, *ACS Catal.*, 2012, **2**, 1765–1772.
68 J. Yu, F. A. Garcés-Pineda, J. González-Cobos, M. Peña-Díaz, C. Rogero, S. Giménez, M. C. Spadaro, J. Arbiol, S. Barja and J. R. Galán-Mascarós, *Nat. Commun.*, 2022, **13**, 4341.
69 T. Ingsel and R. K. Gupta, in *Nanomaterials for Electrocatalysis*, ed. T. Maiyalagan, M. Khandelwal, A. Kumar, T. A. Nguyen and G. Yasin, Elsevier, 2022, pp. 83–111.
70 D. S. Butenko, S. Li, V. O. Kotsyubynsky, V. M. Boychuk, V. I. Dubinko, P. I. Kolkovsky, N. A. Liedienov, N. I. Klyui, W. Han and I. V. Zatovsky, *Int. J. Hydrogen Energy*, 2021, **46**, 21462–21474.
71 B. K. Martini, L. S. Bezerra, S. Artemkina, V. Fedorov, P. K. Boruah, M. R. Das and G. Maia, *Chem. Eng. J. Adv.*, 2022, **9**, 100206.
72 A. Hanan, M. Ahmed, M. N. Lakhan, A. H. Shar, D. Cao, A. Asif, A. Ali and M. Gul, *J. Indian Chem. Soc.*, 2022, **99**(1), 100281.
73 S. Parvin, D. K. Chaudhary, A. Ghosh and S. Bhattacharyya, *ACS Appl. Mater. Interfaces*, 2019, **11**, 30682–30693.
74 R.-Y. Fan, J.-Y. Xie, N. Yu, Y.-M. Chai and B. Dong, *Int. J. Hydrogen Energy*, 2022, **47**, 10547–10572.
75 T. Zhang, S.-A. Liao, L.-X. Dai, J.-W. Yu, W. Zhu and Y.-W. Zhang, *Sci. China Mater.*, 2018, **61**, 926–938.
76 J.-X. Guo, S.-Y. Wu, G.-J. Zhang, L. Yan, J.-G. Hu and X.-Y. Li, *J. Colloid Interface Sci.*, 2022, **616**, 177–188.